RESEARCH ARTICLE

SusMat WILEY

Alternative photothermal/electrothermal hierarchical membrane for hypersaline water treatment

Miao Wang[2] | Wen He[1] | Yuhui Hua[1,4,5] | Xinwen Xie[3] | Shiyan Chen[1,5] | Lei Zhou[3] | Yunmao Zhang[1] | Yaqi Hou[1] | Shihong Lin[6,7] | Haiping Xia[1,4,5] | Jing Zheng[1] | Xu Hou[1,3,5,8,9]

[1]State Key Laboratory of Physical Chemistry of Solid Surfaces, Department of Chemistry, College of Chemistry and Chemical Engineering, Xiamen University, Xiamen, China

[2]College of Materials, Xiamen University, Xiamen, China

[3]Research Institute for Biomimetics and Soft Matter, Fujian Provincial Key Laboratory for Soft Functional Materials Research, Jiujiang Research Institute, College of Physical Science and Technology, Xiamen University, Xiamen, China

[4]Shenzhen Grubbs Institute and Guangdong Provincial Key Laboratory of Catalysis, Department of Chemistry, Southern University of Science and Technology, Shenzhen, China

[5]Collaborative Innovation Center of Chemistry for Energy Materials (iChEM), Xiamen University, Xiamen, China

[6]Department of Civil and Environmental Engineering, Vanderbilt University, Nashville, Tennessee, USA

[7]Interdisciplinary Material Science Program, Vanderbilt University, Nashville, Tennessee, USA

[8]Tan Kah Kee Innovation Laboratory, Xiamen University, Xiamen, China

[9]Engineering Research Center of Electrochemical Technologies of Ministry of Education, Department of Chemistry, College of Chemistry and Chemical Engineering, Xiamen University, Xiamen, China

Correspondence
Haiping Xia and Xu Hou, State Key Laboratory of Physical Chemistry of Solid Surfaces, Department of Chemistry, College of Chemistry and Chemical Engineering, Xiamen University, Xiamen, China.
Email: houx@xmu.edu.cn;
xiahp@sustech.edu.cn

[Correction added on 3 Nov 2022, after first online publication: the sentence waterthe evaporation......interface, and is deleted from second paragraph of introduction section].

Abstract
Over the last decades, the treatment of the large quantities of hypersaline wastewater generated by conventional industries, inland desalination, and fossil-fueled power plants has been an important economic issue and also an inescapable green issue. Here, we developed a versatile interfacial heating membrane with alternating utilization of electricity or solar energy for hypersaline water treatment. This hierarchical membrane functions both as a separation membrane and an interface heater, which can quickly (<0.1 s) convert electricity or solar energy into heat to evaporate the outermost layer of hypersaline water. For 10 wt% hypersaline water, the freshwater production rate can reach 16.8 kg/m^2·h by applying a voltage of 10 V and 1.36 kg/m^2·h under 1-sun illumination. Moreover, it exhibits high electrochemical resistance to corrosion and therefore remains stable tackling hypersaline water (>5 wt%), with a high salt rejection rate of 99.99%. This system shows an efficient desalination strategy that can provide fresh water from brines for agriculture and industry, and even for daily life.

1 | INTRODUCTION

Hypersaline water generally refers to wastewater with salinity not less than 5 wt%, mainly generated by modern industries such as seawater desalination, coal chemical industry, and power generation, et al.[1–6] Currently, most hypersaline water is discharged directly into adjacent open waters, injected into deep underground wells or treated in evaporation ponds,[7,8] which causes serious environmental pollution and waste of a large amount of containing minerals. Therefore, the development of hypersaline water treatment technology is crucial to human survival and the sustainability of the ecological environment. Membrane process (such as reverse osmosis) is a common method to treat saltwater ($\leq$3.5 wt%), but due to the limitation of equipment pressure, the maximum salinity that membrane process can treat is 6 wt%. Moreover, membrane process is unable to avoid material damage caused by salt fouling, thereby reducing desalination performance.[9] For hypersaline water, it is concentrated to near saturation through a concentration system by thermal process and then completely removes all the residual water in the hypersaline water to produce fresh water and solid salt. At present, the commonly thermal treatment of hypersaline water includes multiple effect desalination[10–12] and multistage flash.[13,14] However, this process still has challenges such as large equipment and complex structure, consuming a lot of heat and requiring a large amount of fuel or power supply.[15] Therefore, it is desired to develop a simple and effective instruction with versatile design of membrane to achieve low-cost and efficient hypersaline water treatment.

During thermal process, heat is used to evaporate and concentrate hypersaline water. Since the traditional thermal process needs to heat bulk, while the interfacial heating can concentrate the heat at the gas-liquid interface for evaporation, thereby improving energy utilization.[16–23] During the interfacial heating process, the heat is generated by the membrane that placed on the surface of hypersaline water. Therefore, the membrane should generate heat rapidly to ensure that hypersaline water can be heated and have abundant channels to facilitate the escape of vapor. Carbon nanotubes (CNTs) are excellent material with interfacial heating properties. As previous studies shown, CNTs exhibit a Joule heating effect because of their highly conducting properties[24] and an excellent photothermal effect because of their superior absorption

properties.[25–31] Since solar thermal seawater desalination is unstable due to weather, and the single use of electrical energy will require a large amount of energy input, thereby requiring lots of energy for power generation and causing environmental pollution. If the membrane can synergistically use multiple energy sources to generate heat, it can reduce environmental pollution and be applied in multiple environments. Therefore, it is possible to develop a membrane that can treat hypersaline water by utilizing the interfacial heating properties of CNTs and synergizing multiple energy sources. If the vertically aligned CNTs arrays (VACNTs) are used for hypersaline water treatment, not only sunlight or electrical energy can be utilized, but also abundant channels can be provided for the escape of vapor.

Herein, we designed a multienergy driven evaporation membrane (MDEM) for hypersaline water treatment (Figure 1, Video S1). The structure of MDEM is constructed by vertically aligned micro/nano channels, and photo/electrothermal carbolong complexes (PCCs and ECCs) reported in our previous work[32]; therefore it can alternatively utilize electrical or light energy to generate heat. Moreover, the micro/nano channels within the membrane provide abundant channels for vapor escape, enhancing the desalination capacity. The MDEM offers a promising strategy for wastewater purification by integrating micro/nano structures with photothermal/electrothermal composites.

2 | RESULT AND DISCUSSION

The MDEMs consist of VACNTs and polydimethylsiloxane (PDMS) (Figure 2). VACNTs can provide 6.28 ($\pm$0.31) $\times$ 10^9 nanochannels per square centimeter with diameter of ~55.6 nm as reported in our previous work[33] (Figure S1). PDMS enhanced the mechanical properties of VACNTs. After being washed by NaOH solution, the MDEM kept its original appearance (Figure S2). Furthermore, micropores with a size of 50 μm and density of 130 per square centimeter were formed on this membrane to increase the speed of vapor escape. The carbolong complexes with metal-carbons conjugation were synthesized from the precursor as reported (Figure S3A). The details are described in Supporting Information. The large π-conjugation of PCCs enables them to achieve strong absorption even in the low-energy absorption region, resulting in a good
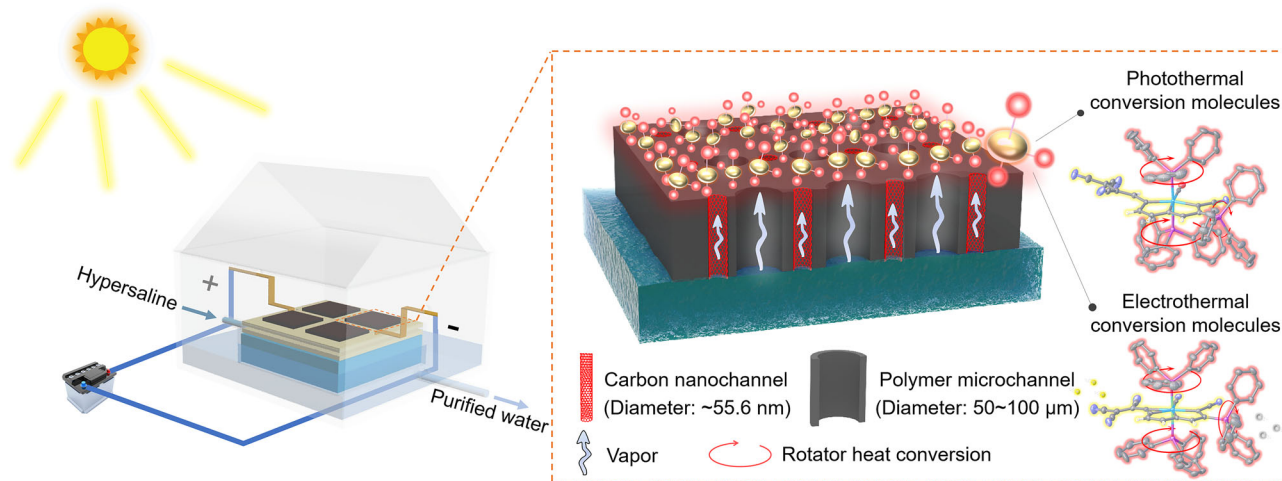
FIGURE 1 *Schematic of alternative hypersaline water treatment system*. The system integrates four multienergy driven evaporation membranes (MDEMs). The MDEM including vertically aligned carbon nanotubes (CNTs) and carbolong complexes with rotator heat conversion effects. The diameter of CNTs nanochannel is about 55.6 nm, and the microchannel is about 50 ~ 100 μm.
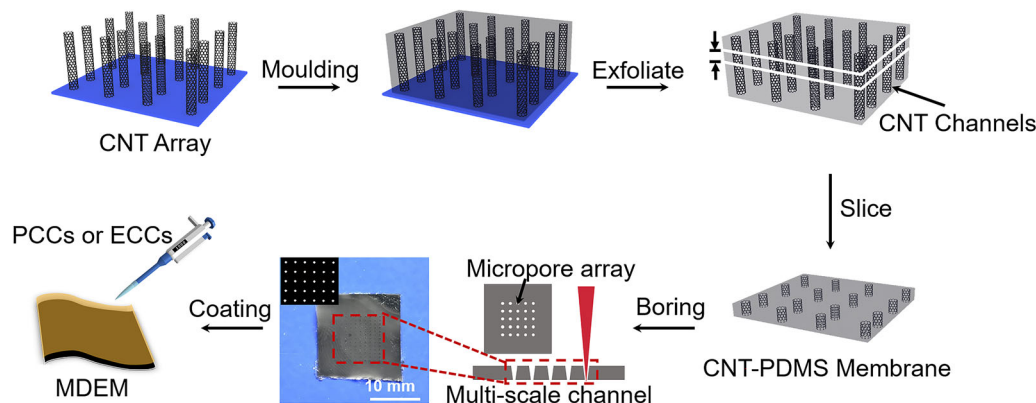

FIGURE 2 *Fabrication of multienergy driven evaporation membrane (MDEM)*. The vertically aligned carbon nanotubes (VACNTs) was encapsulated by polydimethylsiloxane (PDMS). The silicon substrate was removed, and the film was cut with a thickness of 50~100 μm. A porous membrane with 130 pores was obtained by laser cutter. The carbolong complex is coated on the surface of the porous membrane.

photothermal effect (Figure S3B). ECCs exhibit good electrothermal properties, which may be due to their broad excitation energies (Figure S3C). Both PCCs and ECCs were characterized by single X-ray diffraction (Figures S4 and S5). The ultralviolet -visible-near infra-red (UV-Vis-NIR) spectrum (Figures S6 and S7) shows that ECC has high absorption ($\varepsilon > 10^3$) in the wavelength range of less than 1120 nm, while PCC has strong absorption at 661 nm ($\varepsilon = 3.56 \times 10^4$). Under illumination with a light wavelength of 808 nm, the temperature of the ECC and PCC solutions increases with increasing concentration (Figures S8 and S9). The solubilities of the ECC and PCC were investigated to discuss the selection of a suitable solvent for preparing the coating (Tables S1 and S2).

Then, the electrothermal and photothermal properties of the MDEMs were tested. In electrothermal evaporation process, when voltage is applied to MDEM, the CNTs generate Joule heat. The surface temperature of the MDEM increased linearly as the input electrical energy gradually increased (Figure 3A). The surface temperature of the MDEM coated with the ECCs rose exponentially when the voltage gradually increases. The good electrical conductivity of CNTs makes MDEMs have excellent Joule heating effect. Furthermore, MDEM generates the same amount of heat with less energy than MDEM without ECCs due to the excellent electrothermal properties of ECCs. When the input energy is 0.24 W/m^2, the surface temperature of MDEM is 69.3°C, and the surface temperature of MDEM coated with ECCs is 94.7°C. In addition, the MDEM surface was rapidly heated to 50°C in 0.1 s and to 100°C in 0.5 s (Figure S10). The thin film design we adopted enables MDEM to generate heat in a short period of time. Furthermore, even when the thickness is increased to 80 μm, its
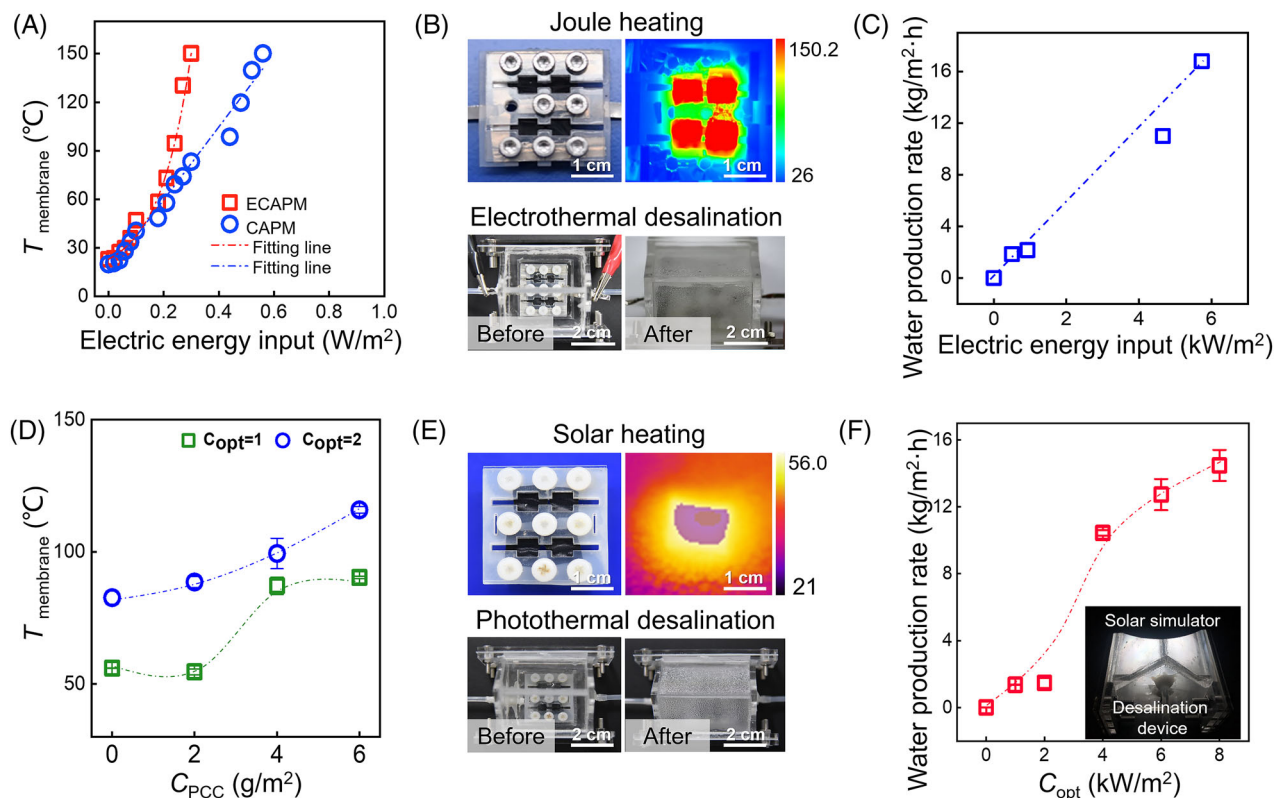
FIGURE 3 *Properties of multienergy driven evaporation membrane (MDEM) and evaporation rates at various energy inputs.* (A) Temperatures of the MDEMs and MDEMs without electrothermal carbolong complexes (ECCs) at different power densities. (B) Image of the desalination device incorporating four MDEMs and an infrared thermal image of the device at 10 V direct current (DC) (upper part). Top-down view of the device before and after Joule heat desalination (bottom part). (C) Relationship between the evaporation rate and input electric energy. (D) Temperature of the MDEM surface at various photo carbolong complexes (PCCs) concentrations and solar illumination densities. (E) Image of the device integrating four MDEMs and an infrared thermal image of the four membranes at a solar illumination of 3 kW/m^2 (upper part). Top-down view of the desalination device before and after 3 kW/m^2 illumination for 30 min (bottom part). (F) Evaporation rate within the integrated device under different solar illumination densities. Error bars represent standard deviations ($n = 3$).

thermal response time remained at 0.1 s due to the fast Joule heating process (Figure S11).

To improve water collection rate, we designed a desalination system integrated with four MDEMs. An electrothermal evaporation test was conducted using a desalination device integrated with MDEMs. In order to ensure the reliability of the results, the following evaporation rate tests (electro/photothermal evaporation) were all carried out in a laboratory with ambient temperature of 25°C and humidity of 70%. Figure 3B shows the integrated device with titanium electrodes connected at both ends. Simulated hypersaline water (10 wt% NaCl solution) was contained in the tank, and the integrated membrane was then placed on the hypersaline water surface. The titanium electrodes penetrated from the side wall of the device and connected to the DC power supply. To avoid electrochemical corrosion, organic silica gel was used to wrap the electrodes to prevent the electrodes from contacting the hypersaline water, thereby avoiding the hypersaline water from being electrolyzed and generating gas bubbles

(Figure S12). At a voltage of 10 V, the surface temperature reached 150°C, which is high enough to cause the water in contact with the MDEMs to evaporate. After 1 h of electrothermal evaporation, there is a large amount of condensation water on the surface of the device (Figure S13). The evaporation rate increases linearly with increasing input energy (Figure 3C). When the input electrical energy was 5.73 kW/m^2, the evaporation rate of MDEMs reached 16.8 kg/m^2·h, showing excellent desalination ability. The surface remains hydrophobic at DC voltages of up to 15 V (Figure S14), which indicated no electro-oxidation of CNTs and high stability of MDEM. Immersion of PDMS avoids the contact of CNTs with water, thereby reducing electro-oxidation.[34]

In terms of photothermal evaporation process, the excellent photothermal effect of CNTs makes the surface temperature of membrane without PCCs reach 56°C under the solar concentration (C$_{opt}$) of 1 kW/m^2 (Figure 3D). Further, the MDEMs has higher temperature at the same C$_{opt}$ due to the photothermal effect of PCCs. And with the increase of
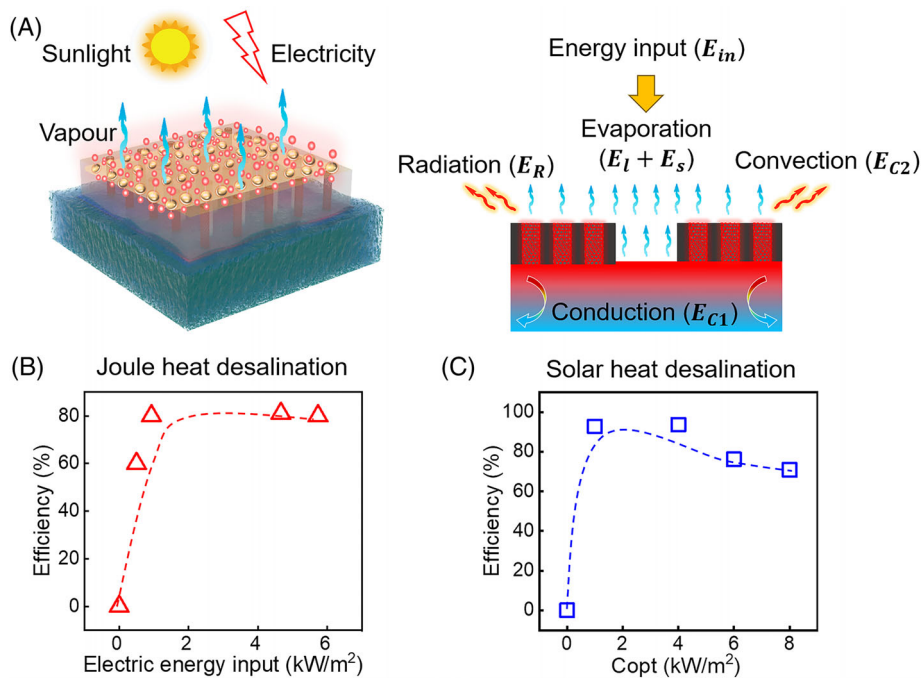
FIGURE 4 *Energy distribution and efficiency*. (A) Schematic showing heat transfer and the energy distribution in multienergy driven evaporation membranes (MDEMs) during photothermal (sun symbol) and electrothermal (lightning bolt symbol) evaporation processes. The blue arrow represents water vapor evaporated by heat. (B) The calculated energy efficiency of Joule heat desalination with different electric energy input. (C) The calculated energy efficiency of solar heat desalination with different solar illumination density. Error bars represent standard deviations ($n = 3$).

the concentration of PCCs, the surface temperature gradually increased. The surface temperature images show that MDEMs has expected photothermal conversion capability and fast thermal response (Figure S15). After irradiating the integrated device with 4 MDEMs under 1 kW/m² for 1 h, a large amount of condensed water was observed on its top (Figure 3E and Figure S16), and the evaporation rate reached 1.36 kg/m²·h. With the assistance of carbolong complexes, MDEMs exhibit superior photothermal or electrothermal properties.

During the above evaporation process, the energy input comes from solar energy or electric energy (Figure 4). For photothermal evaporation, the input energy comes from solar energy. For electrothermal evaporation, electrothermal desalination is carried out by electricity (left part of Figure 4A). The input solar energy or electric energy (Joule heat) of the system is presented by E_{in}. The sensible heat (E_S) refers to the energy required to raise the water temperature, and the latent heat (E_l) refers to the enthalpy of evaporation for a 10 wt% NaCl solution. Usually, the temperature of MDEM is higher than bulk water and air, so heat is lost via conduction (E_{C1}), convection (E_{C2}) and/or radiation (E_R) (right part of Figure 4A). The total input energy can be expressed as Equation (1):

$$E_{in} = E_l + E_S + E_{C1} + E_{C2} + E_R \tag{1}$$

The solar-to-vapor or Joule heat-to-vapor efficiency η is defined as the ratio of the total enthalpy ($E_l + E_S$) to E_{in}, expressed as Equation (2) [35]:

$$\eta = (E_l + E_S)/E_{in} \tag{2}$$

$$E_l = h_v \cdot m \tag{3}$$

$$E_s = C \cdot m \cdot \Delta T, \tag{4}$$

where h_v is the enthalpy of evaporation for the water (2257.2 J/kg); m is the mass of the purified water (g), which represents the mass change rate of water under solar irradiation; C is the specific heat capacity of water (4.2 J/kg·°C); ΔT represents the change in temperature (°C). The evaporation rate (r) was calculated using the Equation (5):

$$r = \frac{m}{A \times t}, \tag{5}$$

where m is the weight loss of water, A is the total area of the four MDEMs, and t is the desalination time.

For the Joule heat desalination process, Q_{in} can be expressed as Equation (6):

$$Q_{in} = U \int I dt, \tag{6}$$

where U represents the voltage (V), I represents the current, $\int Idt$ is the integrated area under the I-t curve, and $U \int Idt$ is the total electrical energy input.

For the solar heat desalination process, Q_{in} can be expressed as Equation (7):

$$Q_{in} = C_{opt} \cdot S \tag{7}$$

where S represents the surface area of the photothermic material.

We calculated the energy efficiency of different electric energy and solar energy inputs. For Joule heat desalination processes, as the input electric energy increased, the Joule heat-to-vapor efficiency first increased and then stabilized. For example, when the electric energy was input at 0.5 kW/m², the Joule heat-to-vapor efficiency was approximately 60%. The energy efficiency reached 80% at an E_{in} of 0.93 kW/m². As the input energy increased to 4.66 kW/m², the Joule heat-to-vapor efficiency increased to 81%. However, as the input energy further increased to 5.73 kW/m², the Joule heat-to-vapor efficiency remained at approximately 80% (Figure 4B). The Joule heat generated by the MDEMs is partially conducted to bulk water, resulting in heat loss, so energy utilization does not increase further with increased input energy. For photothermal desalination, the solar-to-vapor efficiency of 93% and 94% is observed at C_{opt} of 1 and 4 kW/m². With a further increase in C_{opt}, the solar-to-vapor efficiency of MDEMs did not increase further (Figure 4C). Due to heat loss, the energy conversion efficiency η does not increase continuously and remains stable after reaching a maximum value. Therefore, it is necessary to ensure the minimum energy input during the evaporation process and at the same time to achieve the maximum conversion efficiency.

In addition, MDEMs exhibit excellent desalination performance and salt rejection rate when conducted photothermal and electrothermal desalination experiments in simulated hypersaline water (10 wt% NaCl, or $Ca(NO_3)_2$ solution). When the input electrical energy and light density were 5.73 kW/m² and 1 kW/m², respectively, the electrothermal and photothermal evaporation rate of MDEMs is 16.8 kg/m²·h and 1.36 kg/m²·h (Figure 5A,B). After photothermal desalination, the concentrations of Ca^{2+} decreased from 24.39 g/L to 0.04 g/L, and the concentrations of NO_3^- decreased from 75.61 g/L to 0.0001 g/L. The concentrations of these two ions decreased by at least three orders of magnitude. For NaCl solution, the concentration of Cl^- decreased from 60.68 g/L to 1.5 g/L (Figures 5C). After electrothermal desalination, the concentrations of these three ions were significantly reduced. The concentrations of Ca^{2+}, NO_3^- and Cl^- decreased from 24.39 g/L to 0.723 g/L, 75.61 g/L to 0.028 g/L, and 60.68 g/L to 0.11 g/L. The concentration of Cl^- after desalination

meets the standard of agricultural irrigation water (Cl^-: 350 mg/L), and the salt rejection rate reached as high as 99.99%.

When working in hypersaline water, the life of a commercial membrane would be greatly shortened by contamination.[36] Many membrane materials are limited to specific saline concentrations.[37] Under high saline concentrations, the pores of the hydrophilic layer are rapidly plugged by salt deposits; as such, solar evaporation materials need further optimization to efficiently operate under these conditions.[38] To investigate the durability of the MDEM, we tested whether it retains hydrophobicity when desalinating 10 wt% NaCl solution in electrothermal. The contact angle of water on the MDEM was monitored every 30 min, and it remained stable at approximately 130° over 10 cycles (Figure S17A). In addition, the photothermal evaporation rate of the MDEM was determined at a light intensity of 1 kW/m². The evaporation rate was recorded every 30 min during photothermal desalination, and it did not significantly decrease over 10 cycles (Figure S17B). The test results show that MDEM can maintain stable evaporation performance in photothermal or electrothermal desalination cycles with good durability. When treating hypersaline water, the membrane should also have antifouling ability, that is, to avoid clogging of the vapor escape channel due to the adhesion of pollutants. Additionally, we contaminated the MDEM and a commercial polypropylene (PP) membrane with rhodamine B (a fluorescent dye simulating adhering contaminants). The two membranes were then rinsed in ethanol to remove the fluorescent dye. After rinsing, we observed whether any dye remained on the surface of the two membranes and found that the MDEM exhibited no luminescence (Figure S18), which suggests that the porous membrane has excellent antifouling properties.

3 | CONCLUSION

In summary, we have prepared MDEM that can alternatively perform photothermal evaporation or electrothermal evaporation. Then, we introduced a photothermal/electrothermal hypersaline water treatment system based on MDEMs. The superior light-absorption abilities and conductivities of the CNTs and carbolong complexes enable MDEMs to achieve ultrahigh evaporation rate. Moreover, the vertically arranged micro-nanochannels within the membranes play a role in providing abundant channels for water molecules to escape. Our integrated, alternative photothermal or electrothermal hypersaline water treatment system achieves a photothermal freshwater production rate of 1.36 kg/m²·h with energy efficiency of 93% and electrothermal freshwater production rate of
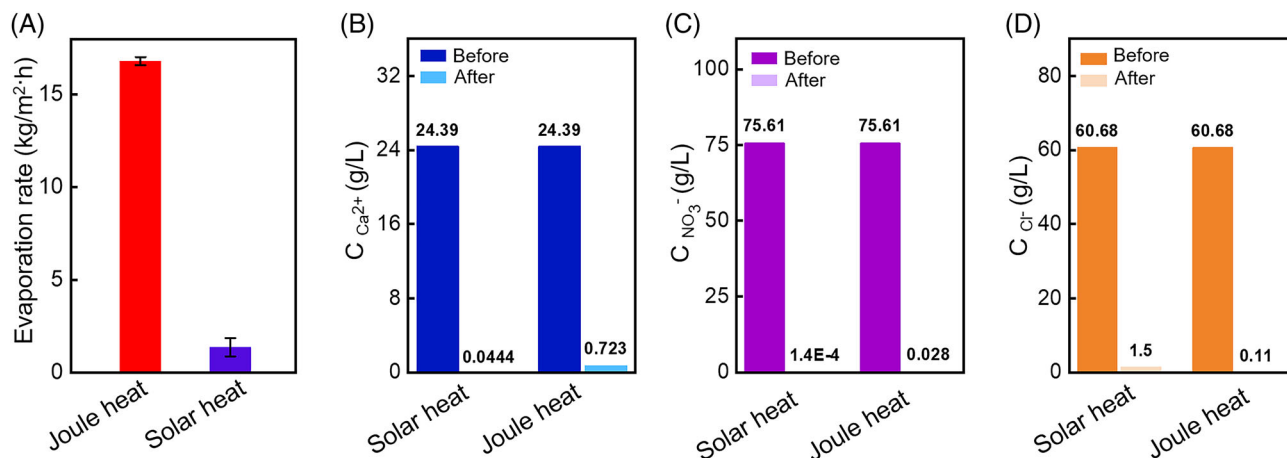
FIGURE 5 *Evaporation rates and salt rejection rates for hypersaline water.* (A) Electrothermal evaporation rate for MDEMs coated with electrothermal carbolong complexes (ECCs) and photothermal evaporation rate for MDEMs coated with photo carbolong complexes (PCCs). (B) Concentration of Ca^{2+} in hypersaline water before and after desalination. (C) Concentration of NO_3^- in hypersaline water before and after desalination. (D) Concentration of Cl^- in hypersaline water before and after desalination. Error bars represent standard deviations ($n = 3$).

16.8 $kg/m^2 \cdot h$ with energy efficiency of 81%. The integrated system can be used to purify hypersaline water samples with a salt rejection rate of 99.99%. After durability tests, the MDEMs show a stable contact angle (130°) and evaporation rate, which means that the membrane has good durability hypersaline water conditions. The conversion of solar energy and electricity into heat in the alternative photothermal or electrothermal hypersaline water treatment system provides an efficient, sustainable, and environmentally friendly strategy for producing fresh water. Many new emerging technologies, such as liquid gating technology,[39] nanofluidic technology,[40] and 3D printing technology,[41] can potential help to further improve the system. We believe that the hypersaline water treatment system will provide ideas for the use of renewable energy and sustainable development.

4 | EXPERIMENTAL SECTION

4.1 | Preparation of the desalination membrane

A multiwalled CNT (MWCNT) array was synthesized by floating catalyst chemical vapour deposition. A silicon wafer with an oxide surface layer was used as the substrate. Xylene was used as the carbon source and introduced at a rate of 6.5 ml/h. Ferrocene (J&K, 99%) was dissolved in xylene (1 g/30 ml) and acted as the catalyst. The carrier gas was argon with the flow rate of 400 cm^3/min. The reaction was carried out over 3 h at 740°C in a tube furnace (OTF-1200X, Hefei Ke Jing Materials Technology Co., Ltd.) to obtain aligned MCNTs with a height of approxi-

mately 500 μm. Xylene and ferrocene were purchased from Sinpharm Chemical Reagent Co., Ltd.

Polydimethylsiloxane (PDMS) (Sylgard 184, Dow Corning Corporation) components A and B were uniformly mixed at a ratio of 10:1, and bubbles were removed in a vacuum drying oven. Then, the MWCNT array was infiltrated by PDMS. After 30 min of permeation, excess PDMS was removed using a spin coating system (Spin-51, Shanghai Chemat Advanced Ceramics Technology Co., Ltd.) operated at 3000 r/min. Then, the composite membrane was solidified at 70°C for 3 h. After solidification, the silicon substrate was removed, and the film was cut with an ultramicrotome (Leica RM2235) to a thickness of 50–100 μm. The micropores were punched with a laser cutter (LEGEND Spirit) at a speed of 2 m/s at 25 W. After this step, a porous CNT array composite membrane with 130 pores in a 5 mm × 5 mm area was obtained, and the pore sizes were 50, 75, and 100 μm. Then, a portion of the membrane was coated with PCC molecules (2 mg/ml) dispersed in solutions with volumes of 100, 200, or 300 μl, while the other portion was coated with the same volume of ECC molecules (2 mg/ml).

4.2 | Desalination device

A photothermal-electrothermal integrated house like device was prepared using polymethyl methacrylate (PMMA), which can alternately perform photothermal and electrothermal desalination. The device includes electrode holes on the side walls, a saltwater tank in the middle of the bottom, and the fresh water tank surrounding the saltwater tank. The integrated structure of

four MDEMs and titanium electrodes was placed on the surface of saltwater tank. Titanium was designed to be interdigitated electrode, so that the four MDEMs were parallelly connected to make the voltage across each MDEM equal. Four MDEMs were bonded to titanium electrodes using conductive silver glue. Then MDEMs-electrodes configuration was sandwiched between two pieces of silicone gasket, and the sandwich structure was encapsulated with two PMMA sheets. Therefore, the integrated structure is assembled into a five-layer structure including PMMA sheet, sandwich structure, and PMMA sheet. Screws were inserted into the corresponding holes slots and tightened. Finally, the electrode tail was penetrated from the device through the electrode holes. When the photothermal desalination process operating, sunlight can pass through the transparent top so that the MDEMs receive enough light and generate heat. When the electrothermal desalination operating, a power supply is connected to the electrode tails, and the MDEMs generate Joule heat.

4.3 | Contact angle test for the MDEM

A fully automatic contact angle and contour analysis instrument (OCA 100, Germany) was used to determine the contact angle of water on the MDEM surface. Water was drawn with a syringe that could automatically deposit a water droplet (5 μl) on MDEM surface and simultaneously monitor the water-membrane contact area. The analysis system was used to determine the contact angle of the water droplet on the membrane surface by analyzing the droplet shape.

4.4 | Infrared thermal images

Temperature changes of the membrane and the integrated device were monitored using an infrared thermal imager (FLIR A325sc).

4.5 | Antifouling performance test

MDEM with the pore size of 50 μm and PP membranes with the pore size of 30 μm were respectively immersed in rhodamine B solution (0.1 mg/ml), then these two membranes were baked in a drying oven (Keelrein DHG-9070A) at 60°C for 5 min. Finally, rhodamine B was eluted with absolute ethanol, and the membranes were dried for fluorescence imaging by a fluorescence microscope (OLYMPUS IX73) with the excitation wavelength of 400 nm.

4.6 | Durability test

Two experiments of membrane durability were performed. In the first experiment, the membranes were placed on the surface of saltwater tank filled with NaCl solution (100 g/L), then the device was heated by the electric heater to 100°C and held at this temperature for 30 min. Finally, the membranes were removed, and their water contact angles were measured. This experiment was repeated 10 times, and 10 contact angle measurements were obtained. In the second experiment, a photothermal evaporation rate test was conducted. The integrated device was irradiated with a light intensity of 1 kW/m^2 for 30 min, and the mass of water lost was determined to calculate the evaporation rate. This experiment was repeated 20 times and lasted a total of 10 h.

4.7 | Electrochemical corrosion resistance test

The MDEM connected to the electrodes was placed on the surface of a 100 g/L NaCl solution, and then a 4 V DC voltage was continuously applied to both ends of the MDEM for 10 h. The digital DC power supply (AB-F SS-L305SPL) was used to record the current change for 10 h. We used the ratio of current to voltage to get the curve of the conductance of MDEM over time during electrothermal desalination process. Then we changed the voltage and tested the current changes over time under voltages of 5 V, 7.5 V, 10 V, and 12.5 V.

4.8 | Salt rejection rate

The salt rejection rate experiments were performed at natural seawater, 100 g/L NaCl and Ca(NO$_3$)$_2$ solution. An ion concentration detector (B&C IC7685) was used to measure the initial concentrations (C_0) and the concentration after desalination (C_1) of Cl$^-$, Ca^{2+}, and NO$_3$$^-$.

The salt rejection rate was calculated using Equation (8):

$$R = \left(1 - \frac{C_1}{C_0}\right) \times 100\% \tag{8}$$

modification. Miao Wang, Wen He, Yuhui Hua, and Xinwen Xie contributed equally to this work.

CONFLICT OF INTEREST
The authors declare no conflict of interest.

ORCID
Yaqi Hou https://orcid.org/0000-0002-9615-9547

REFERENCES

1. Pinto FS, Marques RC. Desalination projects economic feasibility: a standardization of cost determinants. *Renew Sust Energ Rev*. 2017;78:904-915.
2. Gude VG. Desalination and sustainability - an appraisal and current perspective. *Water Res*. 2016;89:87-106.
3. Mansour F, Alnouri SY, Al-Hindi M, et al. Screening and cost assessment strategies for end-of-pipe zero liquid discharge systems. *J Clean Prod*. 2018;179:460-477.
4. Shaffer DL, Arias Chavez LH, Ben-Sasson M, et al. Desalination and reuse of high-salinity shale gas produced water: drivers, technologies, and future directions. *Environ Sci Technol*. 2013;47(17):9569-9583.
5. Córdoba P. Status of flue gas desulphurisation (FGD) systems from coal-fired power plants: overview of the physic-chemical control processes of wet limestone FGDs. *Fuel*. 2017;144:274-286.
6. Shuangchen M, Jin C, Gongda C, et al. Research on desulfurization wastewater evaporation: present and future perspectives. *Renew Sust Energ RevReviews*. 2016;58:1143-1151.
7. Tong T, limelech M. The global rise of zero liquid discharge for wastewater management: drivers, technologies, and future directions. *Environ Sci Technol*. 2016;50(13):6846-6855.
8. Zhang C, Shi Y, Shi L, et al. Designing a next generation solar crystallizer for real seawater brine treatment with zero liquid discharge. *Nat Commun*. 2021;12(1):998-1008.
9. Al-Furaiji M, Arena JT, Ren J, et al. Triple-layer nanofiber membranes for treating high salinity brines using direct contact membrane distillation. *Membranes*. 2019;9(5):60-70.
10. Desale GR, Vasudevan P, Pothal JK. Purification of water using vertical multiple effect distillation unit. *J Sci Ind Res (India)*. 2011;70:634-638.
11. Anand B, Shankar R, Murugavelh S, et al. A review on solar photovoltaic thermal integrated desalination technologies. *Renew Sust Energ Rev*. 2021;141:110787.
12. Quan XY, Luo YQ, Qie SY, et al. Mass transfer during falling film evaporation based on new multi-stage flash model. *J Chem Eng Jpn*. 2015;48(7):528-532.
13. Hamed OA, Al-Sofi MAK, Imam M, et al. Thermal performance of multi-stage flash distillation plants in Saudi Arabia. *Desalination*. 2000;128(3):281-292.
14. Al-Rawajfeh A. Influence of nanofiltration pretreatment on scale deposition in multi-stage flash thermal desalination plants. *Therm Sci*. 2011;15(1):55-65.
15. Said IA, Fuentes N, He Z, et al. Treatment of brackish water reverse osmosis brine using only solar energy. *Environ Sci-Wat Res*. 2021;7(10):1840-1851.
16. Tao P, Ni G, Song C, et al. Solar-driven interfacial evaporation. *Nat Energy*. 2018;3(12):1031-1041.
17. Gao M, Zhu L, Peh CK, et al. Solar absorber material and system designs for photothermal water vaporization towards clean water and energy production. *Energy Environ Sci*. 2019;12(3):841-864.
18. Luo X, Shi J, Zhao C, et al. The energy efficiency of interfacial solar desalination. *Appl Energy*. 2021;302(15):117581.
19. He W, Zhou L, Wang M, et al. Structure development of carbon-based solar-driven water evaporation systems. *Sci Bull*. 2021;66(14):1472-1483.
20. Lu Y, Fan D, Shen Z, et al. Design and performance boost of a MOF-functionalized-wood solar evaporator through tuning the hydrogen-bonding interactions. *Nano Energy*. 2022;95:107016.
21. Zhang L, Li X, Zhong Y, et al. Highly efficient and salt rejecting solar evaporation via a wick-free confined water layer. *Nat commun*. 2022;13(1):849-861.
22. Wu P, Wu X, Wang Y, et al. Towards sustainable saline agriculture: interfacial solar evaporation for simultaneous seawater desalination and saline soil remediation. *Water Res*. 2022;212:118099.
23. Wang Y, Wu X, Wu P, et al. Enhancing solar steam generation using a highly thermally conductive evaporator support. *Sci Bull*. 2021;66(24):2479-2488.
24. Baloch KH, Voskanian N, Bronsgeest M, et al. Remote Joule heating by a carbon nanotube. *Nat Nanotechnol*. 2012;7(5):316-319.
25. Xu J, Zhang J, Fu B, et al. All-day freshwater harvesting through combined solar-driven interfacial desalination and passive radiative cooling. *ACS Appl Mater*. 2020;12(42):47612.
26. Panagiotopoulos NT, Diamanti EK, Koutsokeras LE, et al. Nanocomposite catalysts producing durable, super-black carbon nanotube systems: applications in solar thermal harvesting. *ACS Nano*. 2012;6(12):10475.
27. Xu X, Wan X, Li H, et al. Oil-polluted water purification via the carbon-nanotubes-doped organohydrogel platform. *Nano Res*. 2022;15(6):5653-5662.
28. Hou Y, Wang M, Chen X, et al. Continuous water-water hydrogen bonding network across the rim of carbon nanotubes facilitating water transport for desalination. *Nano Res*. 2021;14(7):2171-2178.
29. Dudchenko AV, Chen C, Cardenas A, et al. Frequency-dependent stability of CNT Joule heaters in ionizable media and desalination processes. *Nat Nanotechnol*. 2017;12(6):557-563.
30. Zhu B, Kou H, Liu Z, et al. Flexible and washable CNT-embedded PAN nonwoven fabrics for solar-enabled evaporation and desalination of seawater. *ACS Appl Mater Interfaces*. 2019;11(38):35005.
31. Qi Q, Wang Y, Wang W, et al. High-efficiency solar evaporator prepared by one-step carbon nanotubes loading on cotton fabric toward water purification. *Sci Total Environ*. 2020;698:134136.
32. Zhu C, Yang Y, Wu J, et al. Five-membered cyclic metal carbyne: synthesis of osmapentalynes by the reactions of osmapentalene with allene, alkyne, and alkene. *Angew Chem Int Ed Engl*. 2015;54(24):7189-7192.
33. Wang M, Meng H, Wang D, et al. Dynamic curvature nanochannel-based membrane with anomalous ionic transport behaviors and reversible rectification switch. *Adv Mater*. 2019;31(11):e1805130.

34. Duan W, Ronen A, Walker S, et al. Polyaniline-coated carbon nanotube ultrafiltration membranes: enhanced anodic stability for in situ cleaning and electro-oxidation processes. *ACS Appl Mater Interfaces*. 2016;8(34):22574.

35. Li X, Zhu B, hu J. Graphene oxide based materials for desalination. *Carbon*. 2019;146:320-328.

36. Li H, Yan Z, Li Y, et al. Latest development in salt removal from solar-driven interfacial saline water evaporators: advanced strategies and challenges. *Water Res*. 2020;177:115770.

37. Fritzmann C, Lowenberg J, Wintgens T, et al. State-of-the-art of reverse osmosis desalination. *Desalination*. 2007;216(1-3): 1-76.

38. Zhang Q, Yi G, Fu Z, et al. Vertically aligned janus MXene-based aerogels for solar desalination with high efficiency and salt resistance. *ACS Nano*. 2019;13(11):13196.

39. Gomollón-Bel F. Ten chemical innovations that will change our world. *Chem Int*. 2020;42(4):3-9.

40. Bocquet L. Nanofluidics coming of age. *Nat Mater*. 2020;19(3): 254-256.

41. Wu L, Dong Z, Cai Z, et al. Highly efficient three-dimensional solar evaporator for high salinity desalination by localized crystallization. *Nat Commun*. 2020;11(1):521-533.

SUPPORTING INFORMATION

Additional supporting information can be found online in the Supporting Information section at the end of this article.